Materials and Design 202 (2021) 109516

Contents lists available at ScienceDirect

Materials and Design

journal homepage: www.elsevier.com/locate/matdes

Impact behavior of nanoengineered, 3D printed plate-lattices

J. Jefferson Andrew [c], Pawan Verma [c,d], S. Kumar [a,b,*]

[a] James Watt School of Engineering, University of Glasgow, Glasgow G12 8QQ, UK
[b] Glasgow Computational Engineering Centre, University of Glasgow, Glasgow G12 8LT, UK
[c] Department of Mechanical Engineering, Khalifa University, Abu Dhabi, United Arab Emirates
[d] Artie McFerrin Department of Chemical Engineering, Texas A&M University, College Station, TX 77840, United States of America

HIGHLIGHTS

- Multi-walled carbon nanotube (MWCNT)-engineered thermoplastic filaments were developed via melt-blending.
- 3D-printed, nanoengineered hybrid plate-lattices exhibit a specific energy absorption (SEA) capacity as high as 19.94 J/g.
- MWCNT-engineered hybrid plate-lattices show superior performance over aluminium and other conventional lattices.
- SEA capacity of 6 wt. % MWCNT loaded plate-lattices is comparable to that of the stainless-steel and titanium lattices.

GRAPHICAL ABSTRACT

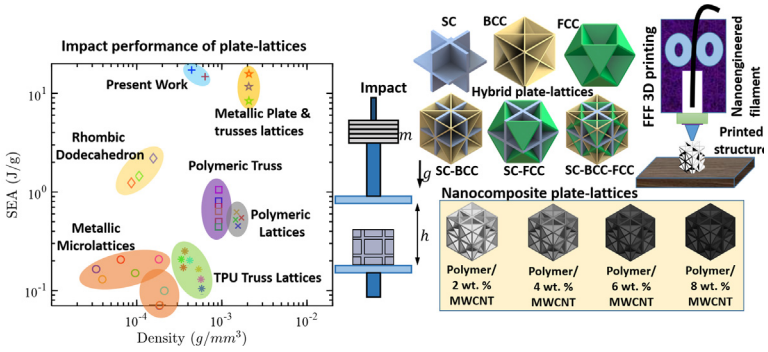

ARTICLE INFO

Article history:
Received 29 November 2020
Received in revised form 20 January 2021
Accepted 21 January 2021
Available online 27 January 2021

Keywords:
Low-velocity impact
Metamaterials
Additive manufacturing
Carbon nanotubes (CNTs)
Polymer cellular composites

ABSTRACT

Herein, we investigate the low-velocity impact behavior of polypropylene random copolymer (PPR)/multi-wall carbon nanotube (MWCNT) and high-density polyethylene (HDPE)/MWCNT plate-lattices processed via fused filament fabrication additive manufacturing, utilizing in-house nanoengineered filament feedstocks. We examine the dynamic crushing and energy absorption characteristics of three typical elementary plate-lattices, namely, simple cubic (SC), body-centered cubic (BCC) and face-centered cubic (FCC) as well as three hybrid plate-lattices (SC-BCC, SC-FCC and SC-BCC-FCC) comprising different weight fractions of MWCNTs at different impact energy levels. The results reveal that the SC-BCC-FCC nanocomposite plate-lattice offers the most favorable impact response as each constituent plate in the lattice contributes to the load carrying capacity for all direction vectors included in the plane of the plate. Furthermore, the results show that impregnating MWCNTs into the PPR and HDPE plate-lattices significantly influences their impact energy attenuation characteristics. Compared with the respective unreinforced plate-lattices, PPR/6 wt% MWCNT SC-BCC-FCC plate-lattices evince higher energy absorption (70%) than HDPE/6 wt% MWCNT SC-BCC-FCC plate-lattices (47%) due to uniform MWCNT dispersion and effective interfacial interaction of MWCNTs in PPR matrix. Our hybrid 3D plate-lattices exhibit a specific energy absorption (SEA) capacity as high as 19.9 J/g, demonstrating their superior impact performance over aluminum and other conventional lattices.

* Corresponding author at: James Watt School of Engineering, University of Glasgow, Glasgow G12 8QQ, UK.
E-mail address: s.kumar@eng.oxon.org (S. Kumar).

https://doi.org/10.1016/j.matdes.2021.109516

1. Introduction

The scope of employing architected materials processed at different length scales (such as nano-, micro-, meso- and macro-architected lattices) is constantly growing in aerospace, marine, automotive, biomedical, and civil sectors [1–4]. Such materials are engineered with distinctive architectural configurations to control and manipulate mechanical stress, sound, light, etc., to explore previously inaccessible mechanical, acoustic, photonic, and several other property spaces [3,4]. Nano- and micro-architected materials, known as metamaterials, represent an emerging class of cellular materials with rationally configured structural hierarchy. In such materials, at each order of hierarchy, the macroscopic properties and relative density are decoupled. Meso- (ligaments size ranging from micron to mm) or macro-architected lattices have been commonly employed as crash energy absorbers in several high-performance engineering applications owing to their remarkable energy absorption properties [3–5]. Depending on the service requirements, both natural and engineered lattices in various topologies and material compositions are utilized [6–8]. Several attempts were made to improve the energy-absorbing characteristics of the architected structures [9] through spatially tailored geometric configurations (e.g., functionally graded cell-walls, corrugation, and spatially tuned semi-apical angles), choice of basis materials (e.g., polymers, metals and composites), and different topologies (e.g., hexagonal, circular, triangular, and square) [2,10,11]. Cellular structures such as honeycombs, and other lattice structures have been widely investigated and evaluated for a huge range of material compositions and topologies [12,13].

Stochastic foams are the first generation manmade isotropic porous materials largely employed for impact energy absorption applications and elastic cushioning [14,15]. Nevertheless, the disadvantage of these materials is that they are stochastic and are composed of random microstructures, resulting in low strength and stiffness properties. As the architecture of these materials plays a vital role in their macroscopic performance and mechanical properties, researchers have developed better replacements for the foam structures. Lattice material is one such developments and can alleviate the limitations of the foams to a great extent. In terms of strength and stiffness, truss-lattices surpass stochastic foams for the same relative density and material property [14,16]. Regardless of their dominance in stiffness to random foams [17], the structural performance of the stiffest truss-lattices is still not the best [12]. For instance, at low relative density, their stiffness achieves below 33% of the Hashin–Shtrikman bound - the maximum theoretically attainable elastic modulus for an isotropic porous solid [13]. Recently, a new group of metamaterials, referred to as plate-lattices are attracting the interest among researchers as they are capable of achieving three times higher stiffness than optimal truss lattices of equal mass [12]. Hybrid lattices (i.e. combination of elementary lattices) can exhibit mechanical properties that are different from the constituent properties and are extremely reliant on both the comparative proportion of solid material and void space (porosity) along with the structural topology (unit-cell architecture). This combination produces an engineered lattice structure capable of providing effective mechanical properties not found in nature [12,18–20].

Among thermoplastic materials, polypropylene (PP) and high-density polyethylene (HDPE) are the most widely used commodity plastics for several industrial applications, mainly owing to their low cost, abundant availability, and ease of processing [21,22]. Moreover, they exhibit relatively high performance/cost ratio, and can be re-used many times devoid of considerable loss of their properties [23,24]. They are remarkably resistant to several chemical solvents, acids and bases [23,25,26]. However, they exhibit an unsatisfying impact behavior (low impact strength and penetration resistance) [26]. This feature limits their application in energy absorbing applications. Several studies focused on modifying them to improve their toughness under dynamic impact loading [27,28]. Different nano or micro fillers and other thermoplastics or elastomers were employed as modifiers to enhance the dynamic energy absorption characteristics of PP/HDPE [29,30]. Factors such as the matrix property, the polymer blend structure, the matrix-filler compatibility and the interfacial adhesion affect the toughening [31,32].

Incorporation of nano-fillers such as multi-walled carbon nanotubes (MWCNTs) has been successfully explored to enhance the matrix dominated properties [33–35]. Moreover, dispersion of MWCNTs in a non-polar polymer matrix such as polypropylene and polyethylene has its own challenges [36]. The main challenge is to evenly disperse them in the polymer matrix [36,37] so as to achieve effective interfacial bonding between the MWCNTs and matrix. The stresses can be effectively transferred from structurally weak matrix to the strong MWCNTs if proper interfacial adhesion is ensured. Effective and efficient stress transfer over and around the matrix/MWCNT interface is vital to obtain superior mechanical properties of resulting polymer nanocomposites [38,39].

The combination of tailored material formulation and complex 3D structural configuration across various scales is hard to accomplish by conventional material synthesis and fabrication techniques. Advanced fabrication methods such as additive manufacturing has enabled fabrication of lattice structures at different length scales (i.e., from nano to macro scale), thereby enhancing their mechanical behavior [40–42]. By leveraging the advantages of emerging 3D printing techniques, lattice structures can be fabricated with ordered, uniform and repeatable microstructure and their unit-cell topologies can be tailored and optimized to achieve the preferred mechanical characteristics for a specific application [43–45].

Herein, we incorporate MWCNTs into meso-architected 3D plate-lattices through nanoengineered filament development and fused filament fabrication to enhance the energy absorption characteristics and to widen the application boundary of PP and HDPE. As summarized above, the extant work on carbon nanostructure incorporated polymer-based plate-lattices is limited. Furthermore, the effect of cell-topology on low-velocity impact behavior of plate-lattices has not been reported in the literature. These outstanding problems deserve a detailed investigation into the assessment of plate-lattices for lightweight applications. For end-use applications, a critical challenge relies on manufacturing and configuring such structures, particularly with required combinations of spatial architecture and material formulation. Therefore, the present investigation focuses on the low-velocity behavior of PPR/MWCNT and HDPE/MWCNT plate-lattices comprising different concentrations of MWCNTs at different impact energy levels.

2. Materials and methodology

2.1. Materials

The polypropylene random copolymer- RA140E (PPR) and high-density polyethylene- Borcoat™ ME0433 (HDPE) thermoplastic materials were supplied by Borouge Pvt. Ltd. The properties of both PPR and HDPE are summarized in Table 1. MWCNTs supplied by Applied Nanostructured Solution, LLC with an average outer diameter of ~10–12 nm and length of less than 30 μm were utilized to produce nano-engineered filaments [46]. The purity of MWCNTs determined from thermogravimetric analysis (TGA) was 86%.

2.2. Melt compounding of nano-engineered filaments for fused filament fabrication

The PPR/MWCNT filament feedstocks with 0, 4, 6 & 8 wt% of MWCNTs and HDPE/MWCNT filament feedstocks with 0, 4 & 6 wt% of MWCNTs were fabricated by melt compounding using a twin-screw extruder (see *Fig. S1* in Supplementary Information). Before compounding, the PPR/MWCNT and HDPE/MWCNT mixtures were vacuum dried at 80 °C for 6 h. For better mixing of MWCNTs with the polymer matrices, both the materials were manually mixed in the presence of acetone solvent. The mixture of HDPE/8 wt% MWCNT nanocomposite couldn't be

Table 1
Properties of PPR (Polypropylene Random Copolymer- RA140E) and HDPE (high-density polyethylene- Borcoat™ ME0433) thermoplastic materials.

Properties	PPR	HDPE
Melt flow index	0.3 g/10 min (230 °C/2.2 kg)	5 g/10 min (190 °C/2.2 kg)
Melting temperature	147.7 °C	134 °C
Crystalline temperature	112.2 °C	109 °C
Crystallinity	30.8%	46.3%

processed owing to the high melt viscosity of the resulting melt-compound. For fabricating the HDPE/MWCNT filaments, the temperature in the 1st, 3rd, 5th, 7th and 9th zone of the extruder was kept at 170, 230, 240, 250, and 250 °C, respectively, while for the PPR/MWCNT filaments, the temperature in the 1st, 3rd, 5th, 7th and 9th zone was kept at 160, 180, 190, 200 and 220 °C, respectively. The screw speed was set to 200 rpm. The polymer nanocomposite filaments were extruded employing a circular die of 1.8 mm diameter. To maintain consistency in the size of the extruded filament, a speed roller was employed. The speed roller helps to alter the filament diameter as per requirement (i.e., ~1.74 mm).

2.3. Fabrication of plate-lattices via FFF 3D printing

Plate-lattice specimens were fabricated using fused filament fabrication (FFF) 3D printing technique, employing a Flash Forge Creator Pro Dual Extrusion 3D Printer equipped with 0.4 mm nozzle on a heated build plate of dimension 215 mm × 215 mm. CAD models of plate-lattices were imported into Simplify3D software (Version 4.1.2) for slicing, and the printing process parameters were customized for the chosen material. The process parameters employed to print the plate-lattice specimens are summarized in *Table* 2. The slicing software generates g-code script depending upon the process parameters employed, which the printer processes to execute the printing. A procedure for optimizing the process parameters to achieve an optimal quality, is employed following [47]. Moreover, printing devoid of support decreases wastage of materials and energy requirements, resulting in reduced printing costs.

Energy absorption characteristics of 3D plate-lattices are highly influenced by their architecture [44]. In this work, six types of topologies, including three elementary structures such as simple cubic (SC), body-centered cubic (BCC) and face-centered cubic (FCC) and three hybrid structures, namely SC-BCC, SC-FCC and SC-BCC-FCC, were investigated. For all the topologies, the relative density, ($\overline{\rho}=\rho/\rho_s$) was set to 36%, where ρ is the density of the cellular structure and ρ_s is the density of the basis material. *Fig. S2* depicts the proportion of various elementary structures in the hybrid plate-lattices. The unit cell configuration, cell design parameters and images of various 3D printed plate-lattice specimens are depicted in Fig. 1. The thickness of the plates in different specimens was varied depending upon the volume of the plates in each lattice configuration to maintain the same relative density. In the hybrid specimens, the elementary structures were combined in an optimal volumetric proportion mentioned in [12], so that their behavior is directional independent in the linear elastic regime. The overall specimens were assembled by eight-unit cells (2 × 2 × 2). The schematics of SC-BCC-FCC plate-lattices with different weight percentages of MWCNTs are depicted in *Fig. S3*. The actual weight of each (kind of) specimen is provided in Table S1.

Table 2
3D printing process parameters employed to fabricate the plate-lattice specimens.

Properties	Standard	Unit
Build Volume	227 × 148 × 150	mm
Layer Resolution	100– 500	microns
Positioning Precision	0.0004	mm
Filament Diameter	1.8	mm
Nozzle Diameter	0.4	mm

2.4. Low-velocity impact tests

Dynamic low-velocity impact tests were performed on the plate-lattice specimens using a CEAST 9350 drop weight impact tower. The impactor employed in the experiments was a flat-faced steel cylinder with a diameter of 60 mm and a mass of 16.7 kg. The lattice specimens were placed on a rigid base to examine the pure dynamic compression behavior under impact load. With such support or boundary conditions, no impact energy can be dissipated through global bending of the lattice specimens. Specimens have been impacted at different impact energies by maintaining a constant impactor mass (16.7 kg). *Table* 3 summarizes the impact heights chosen in this investigation, as well as the corresponding impact velocities and energies.

An optical laser measurement system was employed to measure the velocity during the tests, where the distance moved by the striker between two laser gates is measured as per the principle of triangulation [48]. The real-time variation of the contact force was measured using a dynamic load cell of maximum load capacity 30 kN. CEAST DAS 64 k data acquisition system was used for processing the transient signals acquired by the laser gate and the load cell. The signal sampling frequency of the data acquisition system was set to 3 MSPS (Million Samples per Second). In the data acquisition system, the acquired signals were transformed into corresponding energy, displacement and velocity. To avoid the damage generated owing to multiple impacts after the end of each impact event, a braking device was used to automatically hold the striker. For each configuration, three samples were tested.

Applying Newton's second law, it is possible to estimate the displacement and absorbed energy with respect to time using the force, velocity and time data,

$$\delta(t) = \delta_i + v_i t + \frac{gt^2}{2} - \int_0^t \left[\int_0^{t'} \frac{F(t'')}{m} dt' \right] dt \quad (1)$$

$$E_a(t) = \frac{1}{2} m \left[{v_i}^2 - {v_f}^2(t) \right] + mg\delta(t) \quad (2)$$

Where, δ is the striker displacement, δ_i is the position of the striker, v_i is the initial velocity, m is the striker mass, F is the contact force, v_f is the final velocity and $E_a(t)$ is the absorbed energy at time t.

2.5. Differential calorimetry analysis

The crystalline temperature (see Supplementary Information, S1.3), melting temperature and % crystallinity of both the PPR and HDPE polymers were evaluated by differential scanning calorimetry (DSC). TA instrument (NETZSCH high temperature DSC) was employed to perform the differential scanning calorimetry (DSC) scans of the PPR and HDPE polymers with various weight percentages of MWCNTs under nitrogen atmosphere. For performing DSC analysis, samples of 10 ± 2 mg were heated from ambient temperature to 200 °C at a rate of 10 °C/min and then held at 200 °C for 2 min to remove the thermal history. The sample was subsequently cooled to the ambient condition at a rate of 10 °C/min. The crystallization behavior of the composites was examined from the cooling scans while the melting behavior was examined from the heating scans.

To calculate the percentage crystallinity of the polymer nanocomposites, the following equation was used:

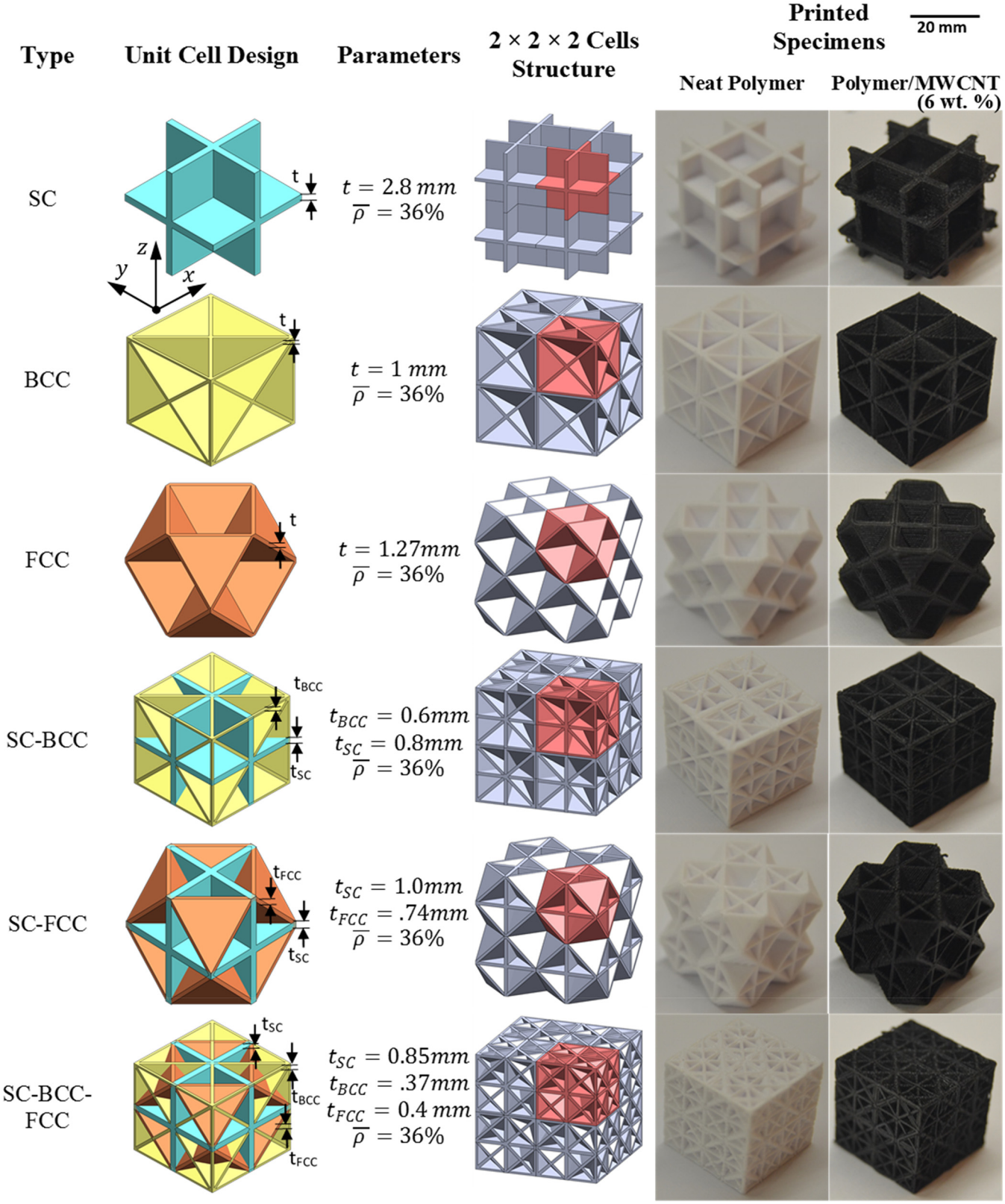

Fig. 1. The unit cell design, cell design parameters, CAD models and printed specimens of various elementary and hybrid plate-lattice structures. Note that all plate-lattices have the same relative density, $\overline{\rho}$ = 36%.

Table 3
Summary of impact height, velocity and the corresponding impact energy.

Impact Height (mm)	Impact Velocity (m/s)	Impact Energy (J)
121.7	1.5	20
182.6	2.4	50
243.5	3.5	100
334.8	4.2	150

$$X_c = \frac{\Delta H_f}{\Delta H_{f0}} \times (1 - w_f) \times 100 \quad (3)$$

Where,
ΔH_f is the melting enthalpy of sample [J/g].
w_f is the weight fraction of filler.
ΔH_{f0} =207 J/g for PPR [49].
ΔH_{f0}=288 J/g for HDPE [49].

3. Results and discussion

3.1. Effect of topology of the plate-lattices

To understand the dynamic behavior of the plate-lattices with different topologies, a series of low-velocity impact tests were performed on the specimens fabricated using neat-PPR filaments. Fig. 2 depicts the contact force-displacement and energy-time responses of selected plate-lattice structures with 36% relative density at an impact energy of 150 J. From these curves, characteristic parameters such as peak contact force, stiffness in the linear regime, displacement and absorbed energy were obtained to characterize the behavior of plate-lattices to drop-weight impacts and to allow comparisons among various plate-lattice configurations. The energy-time curves (Fig. 2b) are shown up to the onset of densification of the specimens. The contact force-displacement curves of different plate-lattices can be categorized into two groups under the same applied impact energy, namely lattices with no rebound (e.g., SC) and lattices with incomplete rebound (e.g., BCC, FCC, SC-BCC, SC-FCC, SC-BCC-FCC) [50].

In general, the contact force-displacement curves depicted an initial linear behavior that was followed by subsequent oscillations (Fig. 2a). In addition, the contact force-displacement curves of all the plate-lattice specimens showed a double-peak. Subsequent to the initial peak, the contact force dropped gradually, signifying some major damage in the structure [50]. Few oscillations, induced by the progressive damage of different ligaments of the structures, occurred before the contact force attained the second peak value [50]. With continued crushing of the specimens by the striker, the contact force response attained a second peak which was higher than the previous one, as a result of densification of the structure. Hence, herein, the absorbed energy was estimated up to the onset of densification of the specimens. The contact force shows a load drop to zero at the end of curve, signifying that the entire impact energy was absorbed in the damage process or rebounded back to the striker [50].

From the impact test results, it is apparent that there is a clear hierarchy in terms of linear stiffness property such that SC>SC-FCC> SC-BCC-FCC >SC-BCC >BCC >FCC. It can be observed that the ranking order of linear stiffness and SC volume content among the plate-lattice systems correlate well, as illustrated in Fig. 2a and *Fig. S1* respectively. It is thus possible that the SC volume content in the plate-lattice structure can affect the liner stiffness of the specimens as the stiffest direction of the SC elementary structure coincides with the loading direction (i.e. high volume of the platelets coincides with the loading direction, hence stiffest among the plate-lattice structures) [12].

Unlike the linear stiffness response regime, the trend was quite different for peak contact force for different plate-lattice configurations. The SC elementary lattices, despite showing highest initial linear stiffness compared to the other plate-lattices (Fig. 2a), exhibited the lowest load tolerance (i.e., low peak contact force) and absorbed energy (Fig. 3). SC specimens were the only plate-lattices to be completely crushed at an impact energy of 36.5 J devoid of exhibiting any energy recovery (Fig. 2a- displacement increases while force decreases – no rebound) [51], while all the other plate-lattices comprised some bending dominated constituent plates [12] showed a slight residual elastic response. For the SC specimens, after the initial peak (Fig. 2a), the contact force-displacement curve showed a long progressively declining plateau mainly owing to severe damage of the vertical plates (*Fig. 4a*). With continued crushing of the specimen, the contact force abruptly raised at the end of the plateau zone to form the second peak prior to dropping rapidly to zero (without any small rebound) at the end of event. In addition, SC specimens were the only plate-lattice specimens to show a significant difference in the contact force between the first and last peak.

From a comparison of the Fig. 2a and *Fig. 4*, it is apparent that the SC specimens were critically damaged during the impact test after the

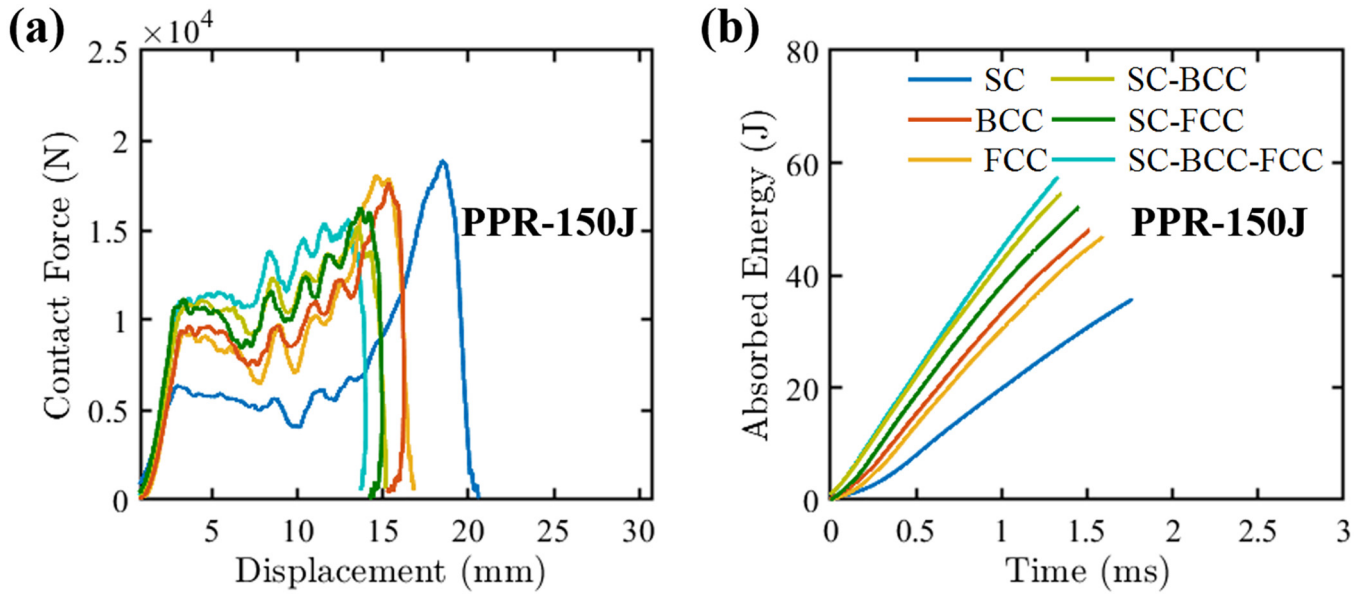

Fig. 2. Measured (a) contact force vs. displacement and (b) energy vs. time histories of different PPR plate-lattice structures (relative density, $\overline{\rho}$=36%) tested at an impact energy of 150 J.

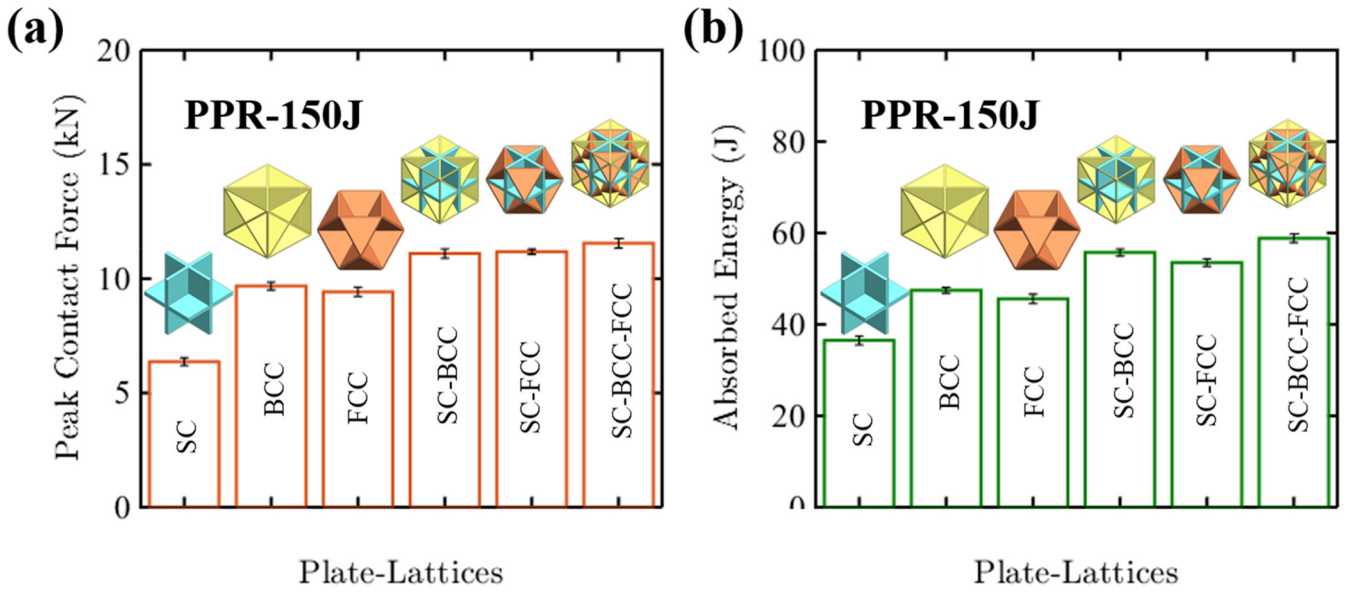

Fig. 3. (a) Peak contact force and (b) absorbed energy of different PPR plate-lattice structures (relative density, $\overline{\rho}$ = 36%) tested at an impact energy of 150 J.

specimens were crushed by about 10 mm (the point at which the compaction/densification initiated) absorbing only about 24.3% of the impact energy (150 J). In this case, the remaining impact energy applied (113.5 J) was dissipated via compaction or densification-an event whose occurrence abruptly increases the load tolerance of the SC plate-lattice [12,50]. For the specimens comprised bending dominated plates (BCC, FCC, SC-BCC, SC-FCC, SC-BCC-FCC), the contact force-displacement curves could be characterized by "incomplete rebound" [50], which had a minor rebound energy at the end of the impact event *(Fig. 2a)*. After the plateau zone, the behavior of the load-displacement curves exhibited different characteristics. Several oscillations with progressively increasing amplitude occurred before the contact force-displacement curve reached the second peak. The occurrence of multiple oscillations in conjunction with minor rebound energy at the end of the impact event suggests that the plate-lattice specimens were not completely crushed or densified [50]. The presence of few intact plates (i.e., no complete densification) in the μCT scans supports experimentally measured macroscopic response (*Fig. 4*). This response apparently suggests that, for the complete densification, the applied impact energy needs to be increased further, indicating the superior energy absorption capacity of these structures [13].

It can be noticed from the Fig. 2a that the SC-BCC-FCC specimens exhibited a lower residual deformation and a higher rebound at the end of the impact event among the specimens consisted of stretch-dominant plates, indicating that the hybrid configuration greatly restricted the damage propagation. As reported by Tancogne et al. [12], the softest direction of the BCC and FCC elementary plate-lattice structures coincides with the stiffest direction of the SC elementary structure, and vice versa. Hence, the superior behavior of SC-BCC-FCC lattice structure is attributed to the fact that each constituent plate in the SC-BCC-FCC lattice structure contributes to the load carrying capacity for all load vectors included in the plane of the plate. Moreover, it is reasonable to suggest that the existence of larger number of open and closed sub-cells in the SC-BCC-FCC structure might have resulted in delaying the premature failure of the lattice structures by more effectual impact damage redistribution as reported in other investigations on various cellular structures (*Fig. S4*) [52,53]. Foregoing discussions revealed the superior impact performance of monolith PPR SC-BCC-FCC plate-lattices. In the sections 3.3 and 3.4, we evaluate the influence of the basis polymer (matrix) chosen and MWCNT content as well as impact energy on the energy absorption characteristics of SC-BCC-FCC plate-lattice structures.

3.2. Differential scanning calorimetry (DSC) analysis

In order to understand the effect of MWCNTs on crystallization (i.e., thermo-physical-mechanical characteristics) behavior of PPR and HDPE polymer matrices (with varying MWCNT loading), DSC analysis were performed. DSC analysis may help to understand the changes in low-velocity impact response of polymers with MWCNT loading as crystallization kinetics of polymer nanocomposites have noticeable effect on the mechanical properties [49,54]. Fig. 5*(a, b)* and Fig. 5*(c, d)* depicts the DSC cooling and heating traces, respectively, for HDPE and PPR with varying amounts of MWCNT content. The DSC heating traces for HDPE and its composites [Fig. 5c] displayed single melting endotherm, while heating traces of PPR and its composites [Fig. 5d] showed double melting endotherm. The appearance of double fusion endotherms in PPR could be either because of previous crystallization conditions (cooling rate) or melting of different lamellar crystals and the presence of crystallites of different sizes. As PPR used in the present study was a copolymer of polypropylene and polyethylene (3–4 wt% of ethylene in PPR) [49], the appearance of double fusion might be due to *co*-polymeric internal morphology of the matrix.

From the DSC scans, peak endothermic temperature/melting temperature (T_m) and peak exothermic temperature (T_c) were determined, and the results are summarized in Tables 4 and 5 for HDPE and PPR, respectively. The DSC results confirmed that the melting temperature, T_m and the crystalline temperature T_c of HDPE and PPR composites increased with MWCNT content. The increase in the T_m and T_c confirmed the nucleating effect and reinforcing action of MWCNTs in polymer matrix. Further, the MWCNT induced thermo-physical changes might be ascribed to the homogenous dispersion of MWCNTs and interfacial adhesion that are crucial for the load transfer from the polymer to the MWCNTs across the MWCNT-polymer interface.

From the area under the endothermic transition (Fig. 5c *and* d), the melting enthalpy (ΔH_f) of different samples were calculated. The results of percentage crystallinity are summarized in Table 4 (for HDPE and HDPE/MWCNT composites) and Table 5 (for PPR and PPR/MWCNT composites). The addition of MWCNTs showed improved crystallization in PPR matrix over HDPE. Overall percent crystallinity of PPR is 30% and HDPE is 46%. Less crystalline structure of PPR provides free volume for filler dispersion. Uniform dispersion of MWCNT provides a load bearing interface and and allows composites to endure a higher impact energy.

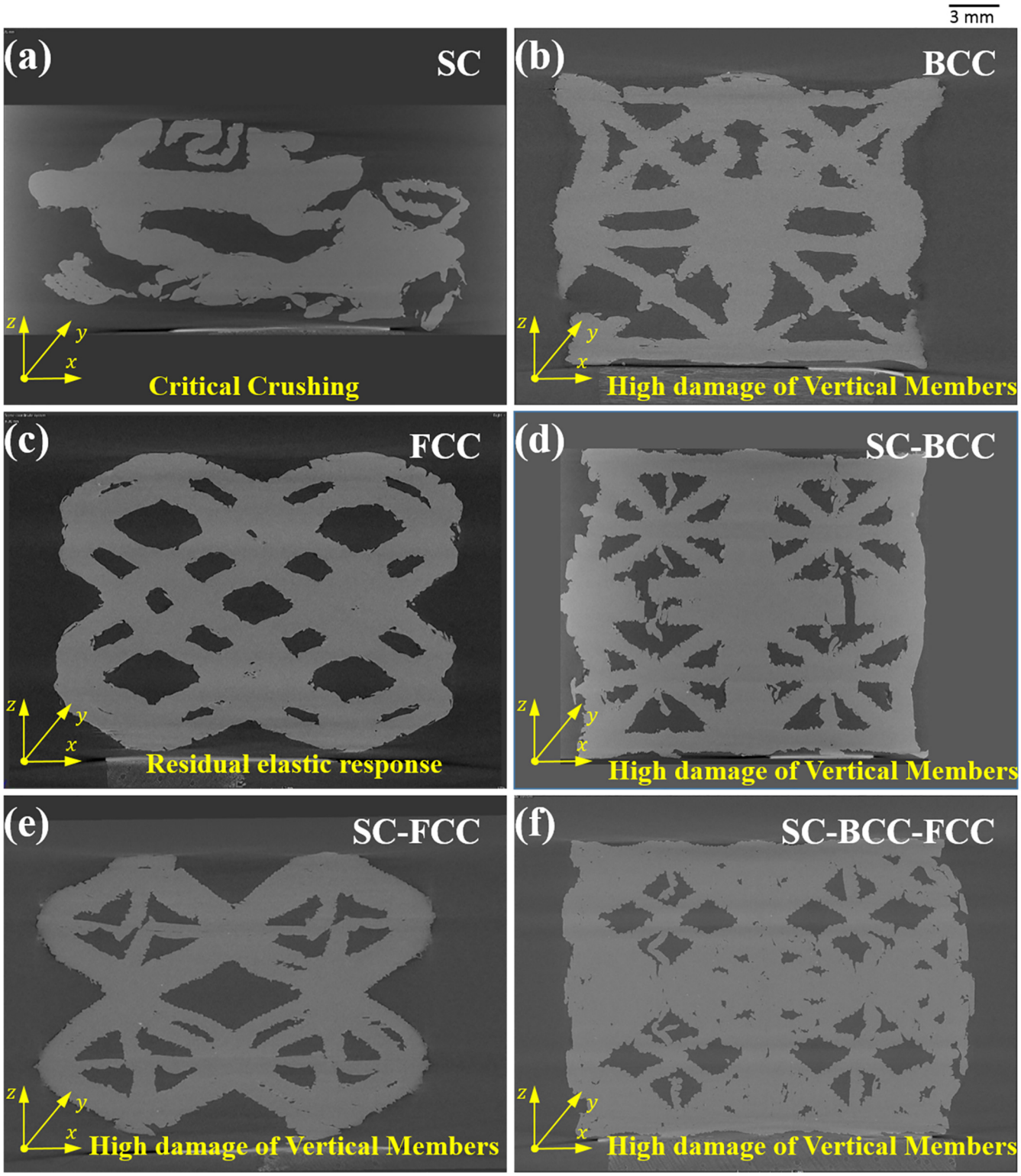

Fig. 4. μCT images of the cross-section of lattices showing impact damage: (a) SC, (b) BCC, (c) FCC, (d) SC-BCC, (e) SC-FCC and (f) SC-BCC-FCC specimens.

In addition, *co*-polymeric nature of PPR might have provided better interaction with the filler as compared to HDPE [54,55].

3.3. Effect of matrix material and MWCNT content on the impact response of SC-BCC-FCC plate-lattices

To study the individual and associated effects of matrix material and MWCNT content on the energy absorption characteristics, the PPR/MWCNT and HDPE/MWCNT SC-BCC-FCC plate-lattices with different weight percentages of MWCNTs were tested at an impact energy of 150 J, and the measured force vs. displacement response and energy vs. time histories are shown in Fig. 6. The peak contact force and absorbed energy acquired from the contact force-displacement and energy-time curves, respectively, are summarized in Fig. 7 for different MWCNT loadings. The results showed that impregnating MWCNTs into the PPR and HDPE polymer matrices considerably changed the impact

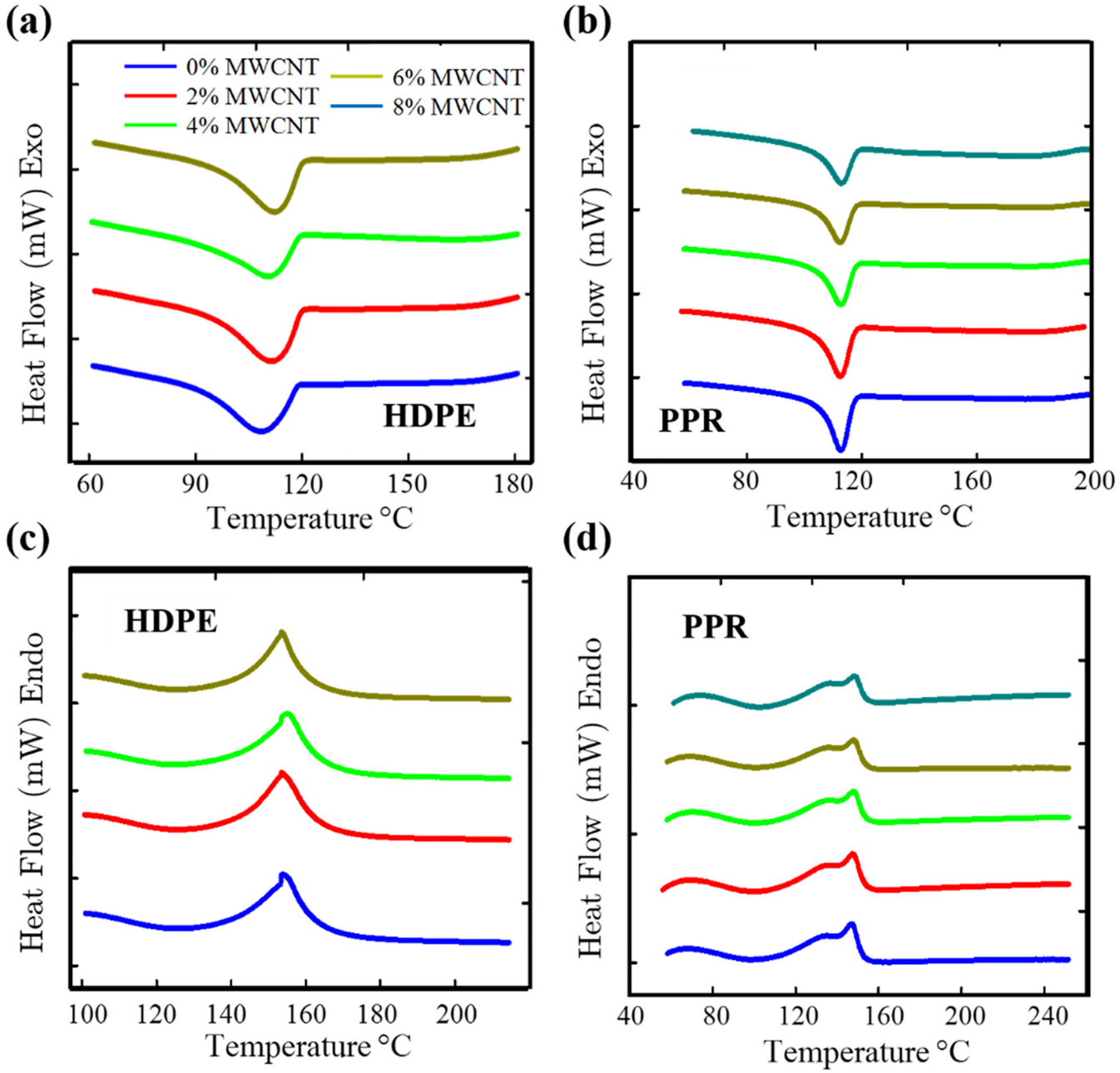

Fig. 5. DSC scans for different polymers and its nanocomposites with varying amounts of MWCNT: cooling scans for (a) HDPE and (b) PPR based nanocomposites and, heating scans for (c) HDPE and (b) PPR based nanocomposites.

Table 4
Effect of MWCNT content on percent crystallinity of HDPE.

Samples	T_m (°C)	T_c (°C)	% Crystallinity
Neat HDPE	133.8	109.1	46.3
HDPE/2 wt% MWCNT	133.5	111.7	46.9
HDPE/4 wt% MWCNT	134.9	110.8	46.2
HDPE/6 wt% MWCNT	133.8	112.2	47.3

energy attenuation characteristics. Indeed, addition of MWCNTs into the polymer matrices leads to improvement in both peak contact force and absorbed energy.

The peak contact force and absorbed energy of neat HDPE SC-BCC-FCC plate-lattice structure were 11.6 kN and 58.8 J, respectively, and with the incorporation of 6 wt% MWCNTs, the peak contact force of HDPE SC-BCC-FCC plate-lattice increased to a maximum of 18.5 kN, exhibiting ~60% increase and the absorbed energy increased to 86.4 J, showing an increase of ~47%. On the other hand, the peak contact force and absorbed energy of neat PPR SC-BCC-FCC plate-lattice structure were 7.9 kN and 42.2 J, respectively, and with the addition of 6 wt% MWCNTs, the peak contact force and absorbed energy of PPR SC-BCC-FCC plate-lattice increased to 12.9 kN (showing an increase of ~61%) and 71.8 J (~70%), respectively. The impact response enhancement of MWCNT reinforced SC-BCC-FCC plate-lattices is a function of (i) the interaction between the polymer and MWCNTs and (ii) total polymer/MWCNT interfacial area [36]. To have a detailed understanding of damage behavior of the nanocomposite plate-lattices under impact loading due to the addition of MWCNTs, SEM images were captured and discussed in Supplementary Information (section *S1.2. Fractography)*.

Table 5
Effect of MWCNT content on percent crystallinity of PPR.

Samples	First Endotherm	Second Endotherm	T_c (°C)	% Crystallinity
	T_{m1} (°C)	T_{m2} (°C)		
Neat PPR	136.0	147.7	112.2	30.8
PPR/2 wt% MWCNT	134.6	147.9	112.5	30.7
PPR/4 wt% MWCNT	134.1	147.8	112.6	30.8
PPR/6 wt% MWCNT	136.1	147.8	113.8	32.4
PPR/8 wt% MWCNT	136.5	148.5	113.0	32.3

The impact performance of the PPR/MWCNT SC-BCC-FCC plate-lattices gradually reduced when the MWCNT content exceeded the critical concentration (i.e., ˃ 6 wt%). The key reasons to this conflicting observation are the poor printing quality of the plate-lattice specimens and agglomeration of MWCNTs at high MWCNT loading. In FFF 3D printing, MWCNT, at high loading, turns out to be unstable in the polymer melt and thus affects the flow behavior owing to the MWCNT induced viscosity [56]. This in turn results in poor printing quality. Moreover, at higher MWCNT loading, polymer nanocomposites exhibit agglomeration due to strong van der Walls force of attraction. It can also be seen from Table 5 that the crystallinity of PPR nanocomposites at higher loading is almost same as that at lower loading. This is probably due to agglomeration of MWCNTs at higher loading. Due to this, the availability of MWCNTs for nucleation of polymer crystals is almost

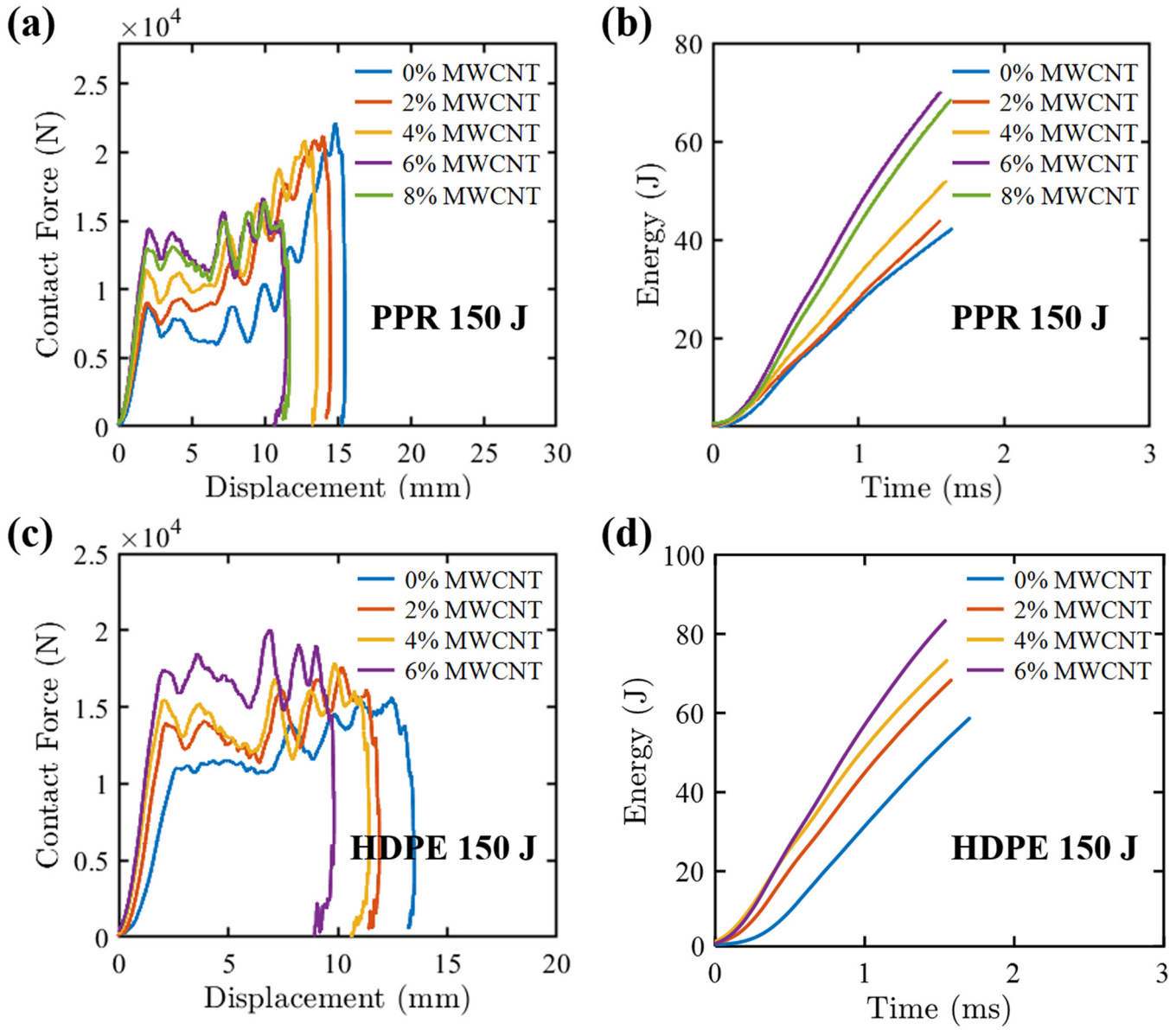

Fig. 6. Measured force vs. displacement and energy vs. time histories of (a, b) PPR/MWCNT and (c, d) HDPE/MWCNT composite SC-BCC-FCC plate-lattices with different weight percentages of MWCNTs (0, 2, 4, 6 and 8 wt%) tested at an impact energy of 150 J.

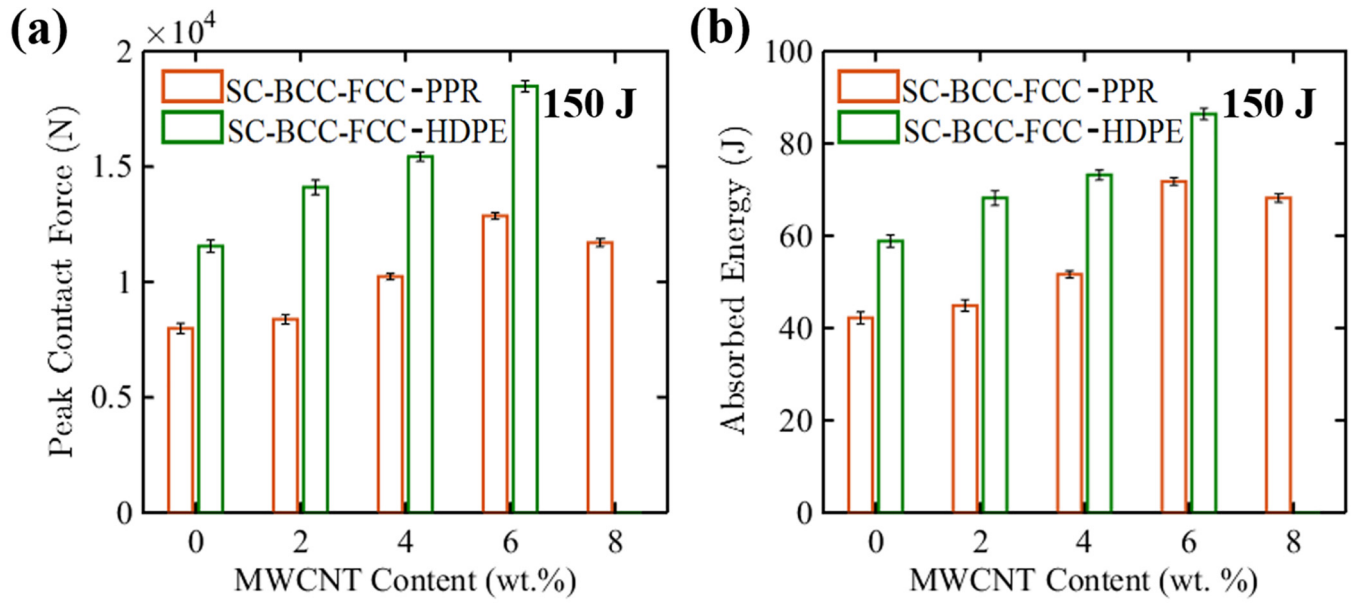

Fig. 7. (a) Peak contact force and (b) absorbed energy of PPR/MWCNT and HDPE/MWCNT SC-BCC-FCC plate-lattices with different weight percentages of MWCNTs (0, 2, 4, 6 and 8 wt%) tested at an impact energy of 150 J.

the same as that at lower loading. Hence, at higher loading, MWCNT is not contributing to crystallinity increment but it increases the viscosity of composites. Fig. 8 depicts the dispersion state of MWCNTs in the PPR and HDPE matrices for different loadings of MWCNT. Uniform dispersion of MWCNTs in the matrix are observed for 2, 4 and 6 wt% PPR/MWCNT and HDPE/MWCNT nanocomposite SC-BCC-FCC structures. SEM microstructure analysis of the PPR/8 wt% MWCNT printed samples (Fig. 9b) confirmed that MWCNTs are randomly aligned within the PPR matrix with some traces of MWCNT agglomerations. Interestingly, on the other hand, SEM microstructure analysis of the composite filament (PPR/8 wt% MWCNT, Fig. 9a) showed uniform dispersion of MWCNTs in the polymer matrix. The printing induced defects and agglomeration of MWCNTs in the PPR polymer matrix of printed lattices might be responsible for the decrease in the impact performance at higher loading of the MWCNTs [36].

Uniform dispersion of reinforcements in polymer matrix is a prerequisite for enhancement in mechanical response of the composite materials [36]. This constraint is usually in discrepancy with the necessity for higher weight fraction of reinforcing MWCNTs. The toughening mechanisms, such as crack bridging, crack deflection and fiber pull-out [36]

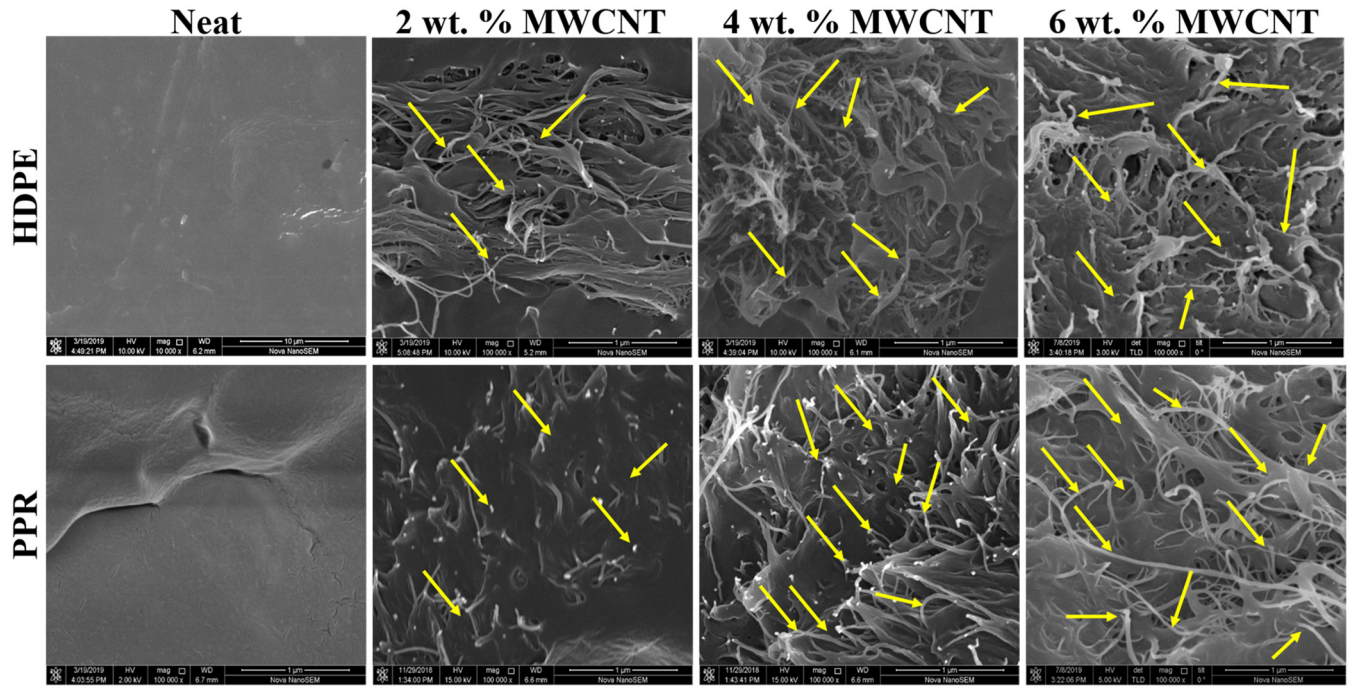

Fig. 8. SEM micrographs of 3D printed SC-BCC-FCC structures depicting the surface morphologies of HDPE, PPR and its nanocomposites for different wt% of MWCNTs (arrows indicate MWCNTs).

occurs predominantly only in the absence of agglomerates. Moreover, aggregated MWCNTs results in stress concentration [36]. Agglomeration due to the addition of more than 6 wt% MWCNTs into the PPR matrix, decreases the effective interfacial area in PPR/MWCNT composite plate-lattices, leading to decreased mechanical performance.

In order to explicitly report the effect of polymer/MWCNT interaction on the energy absorption characteristics, the normalized absorbed energy of HDPE/MWCNT and PPR/MWCNT SC-BCC-FCC plate-lattices were evaluated as the ratio of the absorbed energy of the MWCNT loaded specimen to the absorbed energy of the corresponding neat specimen. Fig. 10 depicts the normalized absorbed energy as a function MWCNT content in the HDPE/MWCNT and PPR/MWCNT plate-lattices. Up to 4 wt% MWCNT, the HDPE/MWCNT SC-BCC-FCC plate-lattices showed higher normalized absorbed energy compared to the PPR/MWCNT lattices. It is interesting to note that the ranking order of the absorbed energy between the neat HDPE and PPR specimens were the same as for 2 and 4 wt% MWCNT content. It is as a result possible that the inherent properties of the HDPE polymer matrix might have played a predominant role on the impact characteristics of nanocomposite plate-lattice structures. In contrast, for 6 wt% MWCNT content, the PPR specimens surpassed HDPE ones in terms of the normalized absorbed energy. This result might be ascribed to relatively strong interfacial interaction between the PPR matrix and MWCNT as well as efficient stress-transfer between them through the subtle polymer/MWCNT interface [36], as shown in Fig. 10.

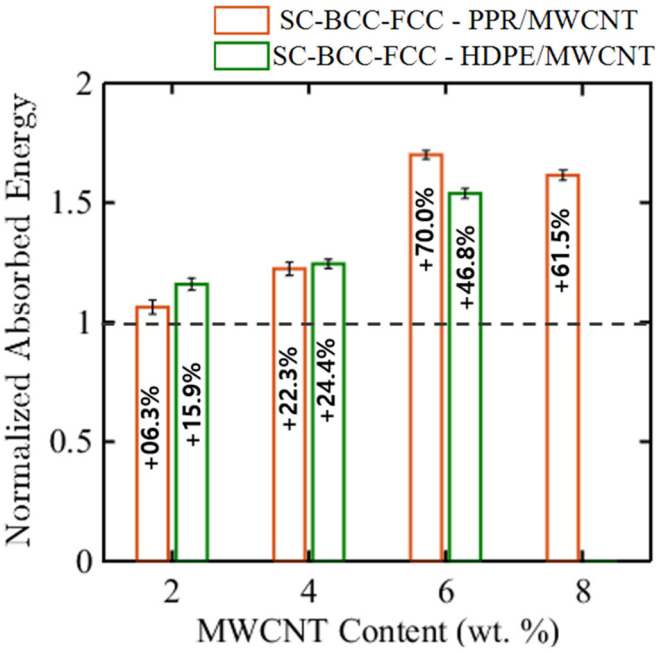

Fig. 10. Normalized absorbed energy (with respect to respective neat PPR and HDPE lattices) as a function of increasing MWCNT weight percentage in the HDPE/MWCNT and PPR/MWCNT SC-BCC-FCC plate-lattices.

3.4. Effect of impact energy

Typical contact force vs. displacement plots for HDPE and PPR SC-BCC-FCC plate-lattices (with 0 and 6 wt% MWCNTs) tested at impact energy levels of 20, 50, 100 and 150 J are depicted in Fig. 11 and Fig. 12, respectively.

The HDPE/MWCNT and PPR/MWCNT SC-BCC-FCC plate-lattices showed better performance in terms of linear stiffness, peak contact force and absorbed energy in comparison to corresponding unreinforced ones, irrespective of the impact energy level. Moreover, all MWCNT reinforced specimens depicted a residual resistance after impact, as confirmed by the small rebound of the impactor at the end of impact event [50]. Also, subjecting the MWCNT reinforced HDPE and PPR specimens to higher impact energies did not result in complete compaction/densification (in contrast to that observed for the neat HDPE and PPR specimens), but in stable and continuous crushing of different plate-lattices, evident from the continuous increase in duration of the oscillating plateau region with increasing impact energy level. However, the impact response of HDPE/MWCNT and PPR/MWCNT plate-lattices were different and this behavior further changed with the impact energy levels.

At impact energy level of 20 J (Fig. 11a), the contact force history curves of neat HDPE and HDPE/MWCNT SC-BCC-FCC plate-lattices were very similar (i.e., showed rebounding behavior). The contact force-displacement curves of neat HDPE specimens impacted at 50 J showed a different behavior characterized by "incomplete rebound", which had a long oscillating plateau and a small rebound at the end of the event (Fig. 11b). The peak of the neat HDPE specimens started to converge to a value of about 11 kN at impact energies ≥50 J, while those of HDPE/MWCNT specimens showed a monotonic increase until up to impact energy of 100 J (started to converge to a value of about 20 kN at 100 J). For the case of neat HDPE specimens at 150 J

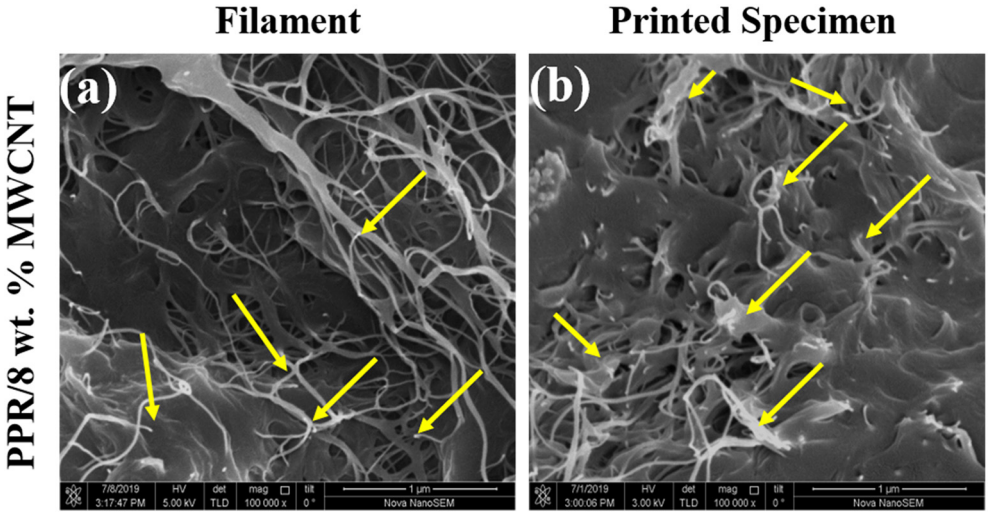

Fig. 9. Dispersion state of 8 wt% MWCNTs in (a) PPR filament and (b) 3D printed SC-BCC-FCC PPR/MWCNT structures.

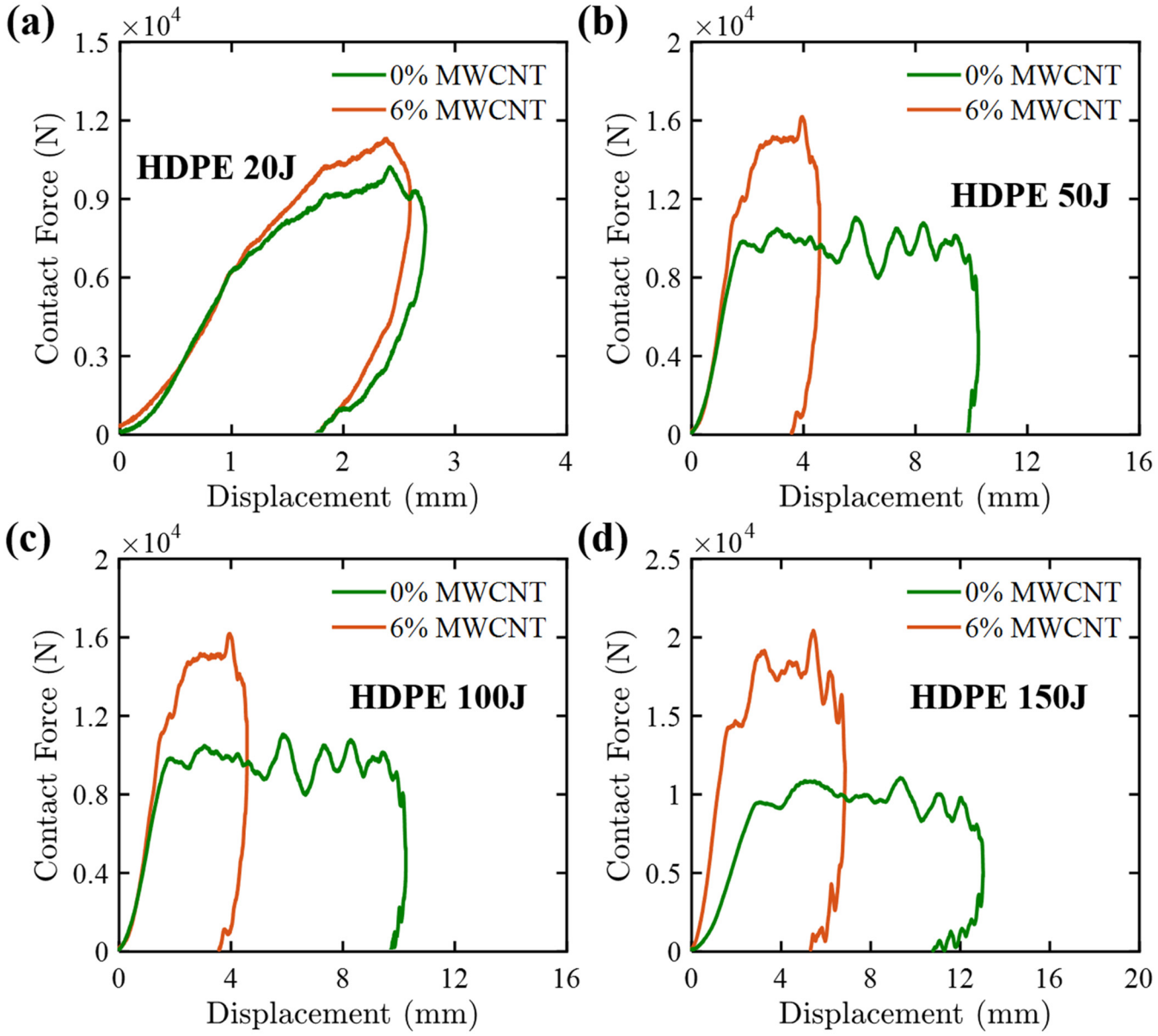

Fig. 11. Typical force vs. displacement response of neat HDPE and HDPE/ 6 wt% MWCNT SC-BCC-FCC plate-lattices tested at impact energies of (a) 20 J, (b) 50 J, (c) 100 J and (d) 150 J.

(Fig. 11d), the contact force increased following almost a non-linear and oscillating pattern after the plateau region, corresponding to the absorption of most of the remaining impact energy through densification process. At the same impact energy level, no sign of complete densification was noticed in the case of HDPE/MWCNT plate-lattices.

The PPR-based specimens (Fig. 12) exhibited, compared to HDPE-based specimens, an impact performance drop with increasing impact energy levels. The PPR and PPR/MWCNT specimens exhibited a sort of saturation of the peak contact force starting from 20 and 50 J, respectively. For the neat PPR specimens, the densification process initiated at an impact energy level of 100 J. For the PPR/MWCNT specimens, on the other hand, the duration of oscillating plateau region increased steadily with increasing impact energy (i.e., up to 150 J).

From a comparison of the experimental curves of the MWCNT reinforced HDPE and PPR SC-BCC-FCC plate-lattices presented in Figs. 11 and 12, it is apparent that the residual displacement (i.e., permanent deformation) of the PPR/MWCNT specimens were significantly higher than the HDPE/MWCNT ones even at the impact energy level of 20 J. The difference in residual displacement between the PPR/MWCNT and HDPE/MWCNT specimens significantly increased with increase in impact energy. Moreover, for the impact energies up to 100 J, the contact force-displacement curves of HDPE/MWCNT specimens revealed a significant elastic rebound phase, characterized by a single peak (i.e., devoid of many oscillations) with an almost enclosed shape curve. On the other hand, the PPR/MWCNT specimens showed such response only at impact energy level of 20 J, indicating the poor restriction to damage progression at higher impact energies. The better rebounding behavior in conjunction with lower residual deformation of HDPE/MWCNT specimens at higher impact energy levels indicates their superior energy absorption behavior [51].

3.5. Comparative energy absorption characteristics of hybrid plate-lattices

Form Fig. 13, it is clear that the PPR/6 wt% MWCNT and HDPE/6 wt% MWCNT SC-BCC-FCC plate-lattices exhibit a specific energy absorption (SEA) capacity of 16.1 and 19.9 J/g, respectively, demonstrating comparable performance of our hybrid plate-lattices to that of the stainless-

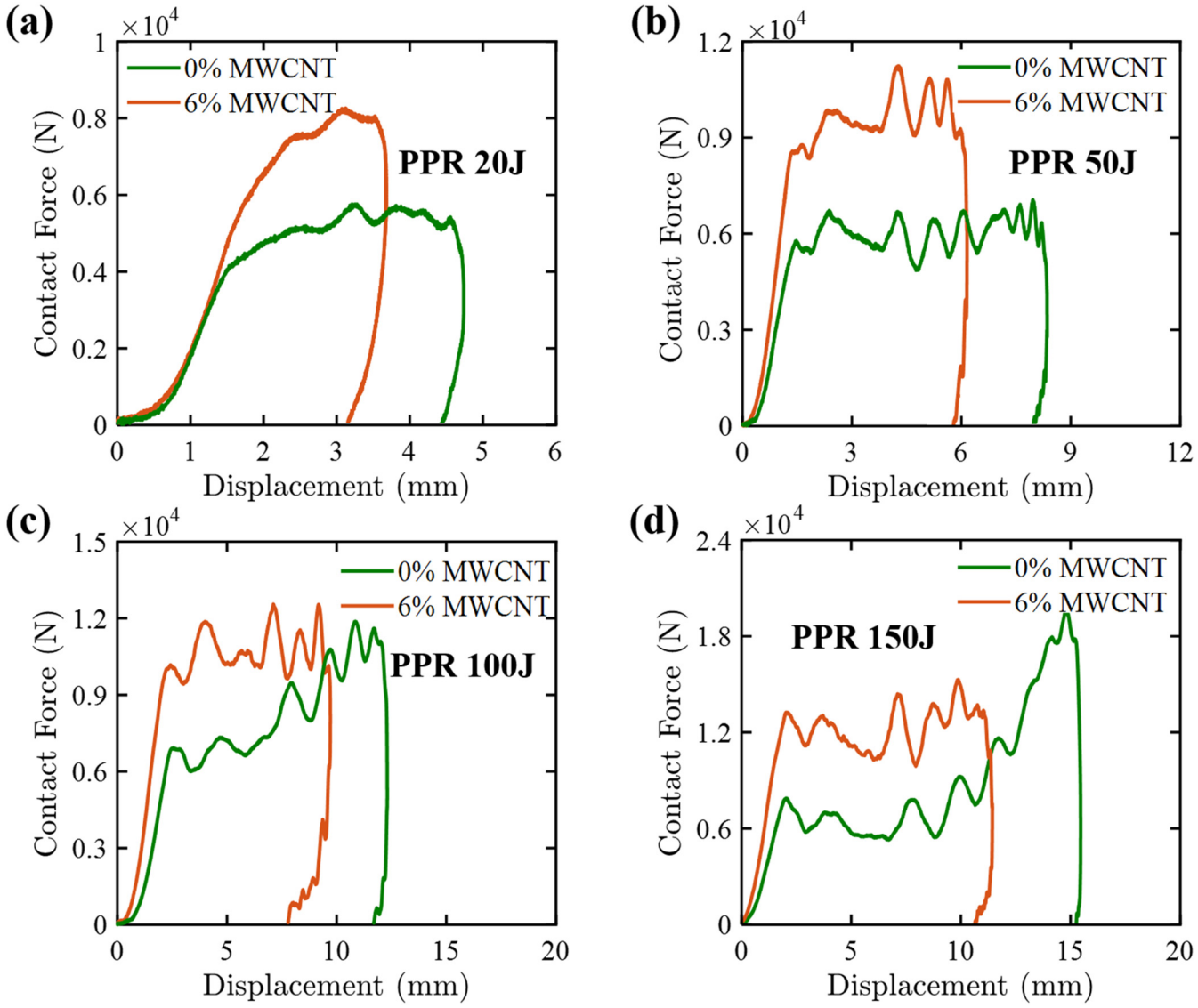

Fig. 12. Typical force vs. displacement response of neat PPR and PPR/ 6 wt% MWCNT SC-BCC-FCC plate-lattices tested at impact energies of (a) 20 J, (b) 50 J, (c) 100 J and (d) 150 J.

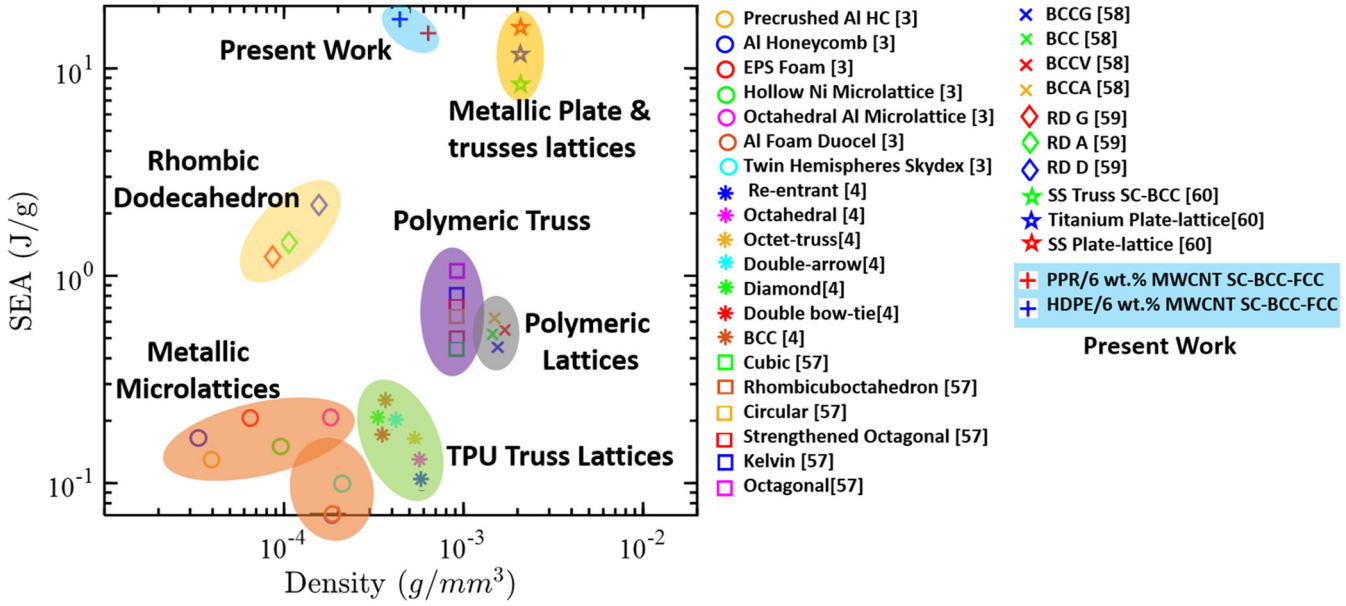

Fig. 13. Comparison of specific energy absorption (SEA) capacity of the carbon nanostructure engineered hybrid SC-BCC-FCC plate-lattices with the extant literature [57–60].

steel and titanium lattices. Moreover, the SEA of these lattice structures is higher than that of the aluminum and other conventional lattices, as shown in Fig. 13. It is noteworthy that fabrication of the lattice structures based on stainless-steel and titanium involves expensive processes such as EBM, laser cladding, etc. as compared with the cost-effective FFF approach employed in this study.

4. Conclusions

In this study, the low-velocity impact behavior of PPR/MWCNT and HDPE/MWCNT plate-lattices processed via FFF additive manufacturing , utilizing in-house developed filament feedstocks, was investigated. Three typical elementary (SC, BCC and FCC) and three hybrids (SC-BCC, SC-FCC and SC-BCC-FCC) nanocomposite plate-lattices with different weight fractions of MWCNTs were tested and the dynamic crushing and energy absorption characteristics of such mesoarchitected composite lattices at different impact energy levels were evaluated. The following key conclusions can be drawn from the experimental results:

1. The SC-BCC-FCC plate-lattice offered the most favorable impact response as each constituent plate in the lattice contributed to the load carrying capacity for all direction vectors included in the plane of the plate.
2. The morphological signatures of plate-lattice specimens with both stretch- and bend-dominated plate-lattices (SC-BCC, SC-FCC and SC-BCC-FCC) showed more progressive damage growth (slow crack evolution) by alternating sequences of cracking and stoppage.
3. Impregnating MWCNTs into the PPR and HDPE plate-lattices considerably changed their ability to attenuate impact energy, leading to improvement in both peak contact force and absorbed energy.
4. Addition of MWCNTs into the polymer matrices restricted the onset or propagation of crack through crack bridging, nanotube pullout and crack deflection damage modes and hence, improved the energy absorption characteristics of the structure.
5. Compared with the respective neat polymer lattices, the improvement in absorbed energy of PPR/MWCNT SC-BCC-FCC plate-lattices (70%) was higher than the HDPE/MWCNT SC-BCC-FCC plate-lattices (54%) due to higher nucleating effect of MWCNTs in PPR matrix compared to that in HDPE matrix.
6. The performance of nano-engineered SC-BCC-FCC plate-lattices on par with is on par with the stainless-steel and titanium lattices and superior to aluminum and other conventional lattices.

The confluence of emerging additive manufacturing techniques and the ability to design nano- and micro-architected cellular composites will enable the realization of a revolutionary class of metamaterials with unprecedented properties.

Declaration of Competing Interest

The authors declare no conflict of interest.

Acknowledgments

Authors would like to thank to Abu Dhabi National Oil Company (ADNOC) for providing the research grant (Award No: EX2016-000010).

Appendix A. Supplementary data

Supplementary data to this article can be found online at https://doi.org/10.1016/j.matdes.2021.109516.

References

[1] J.J. Andrew, et al., Impact performance enhancement of honeycombs through additive manufacturing-enabled geometrical tailoring, Int. J. Impact Eng. 134 (2019) 103360.
[2] J. Ubaid, B.L. Wardle, S. Kumar, Bioinspired compliance grading motif of mortar in nacreous materials, ACS Appl. Mater. Interfaces 12 (29) (2020) 33256–33266.
[3] T.A. Schaedler, et al., Designing metallic microlattices for energy absorber applications, Adv. Eng. Mater. 16 (3) (2014) 276–283.
[4] F. Shen, et al., Energy absorption of thermoplastic polyurethane lattice structures via 3D printing: modeling and Prediction, Int. J. Appl. Mech. (2016) 08.3.
[5] S. Kumar, et al., Tunable energy absorption characteristics of architected honeycombs enabled via additive manufacturing, ACS Appl. Mater. Interfaces 11 (45) (2019) 42549–42560.
[6] F. Alam, et al., Microarchitected 3D printed polylactic acid (PLA) nanocomposite scaffolds for biomedical applications, J. Mech. Behav. Biomed. Mater. 103 (2020) 103576.
[7] G. Villanueva, W.J. Cantwell, The high velocity impact response of novel fiber-reinforced aluminum foam sandwich structure, Compos. Sci. Technol. 1 (2004) 35–54.
[8] J.F. Davalos, et al., Modeling and characterization of fiber-reinforced plastic honeycomb sandwich panels for highway bridge applications, Compos. Struct. 52 (3) (2001) 441–452.
[9] Z. Ozdemir, et al., Energy absorption in lattice structures in dynamics: experiments, Int. J. Impact Eng. 89 (2016) 49–61.
[10] E. Cetin, C. Baykasoğlu, Energy absorption of thin-walled tubes enhanced by lattice structures, Int. J. Mech. Sci. 157-158 (2019) 471–484.
[11] H. Lei, et al., Evaluation of compressive properties of SLM-fabricated multi-layer lattice structures by experimental test and μ-CT-based finite element analysis, Mater. Des. 169 (2019) 107685.
[12] T. Tancogne-Dejean, et al., 3D plate-lattices: an emerging class of low-density metamaterial exhibiting optimal isotropic stiffness, Adv. Mater. 30 (45) (2018) 1803334.
[13] C. Crook, et al., Plate-nanolattices at the theoretical limit of stiffness and strength, Nat. Commun. 11 (1) (2020) 1579.
[14] W. Lee, Cellular solids, structure and properties, Mater. Sci. Technol. 16 (2) (2000) 233.
[15] K. Stöbener, et al., Aluminum foam-polymer hybrid structures (APM aluminum foam) in compression testing, Int. J. Solids Struct. 45 (21) (2008) 5627–5641.
[16] J.L. Grenestedt, Effective elastic behavior of some models for perfect cellular solids, Int. J. Solids Struct. 36 (10) (1999) 1471–1501.
[17] G. Gurtner, M. Durand, Stiffest elastic networks, Proceed. Royal Soc. A 470 (2164) (2014) (p. 20130611).
[18] J. Berger, H. Wadley, R. McMeeking, Mechanical metamaterials at the theoretical limit of isotropic elastic stiffness, Nature 543 (7646) (2017) 533.
[19] Z. Chen, et al., Novel negative poisson's ratio lattice structures with enhanced stiffness and energy absorption capacity, Materials 11 (7) (2018) 1095.
[20] R. Gautam, I. Sridhar, Compressive properties of additively manufactured functionally graded Kagome lattice structure, Metals 9 (5) (2019) 517.
[21] R. Vinny, Sastri, 3 - Materials used in medical devices, in: Vinny R. Sastri (Ed.), Plastics in Medical Devices, Second ed.William Andrew Publishing 2014, pp. 19–31.
[22] P.K. Mallick, 1 - Overview, in: P.K. Mallick (Ed.), Woodhead Publishing Series in Composites Science and Engineering, Materials, Design and Manufacturing for Lightweight Vehicles, Woodhead Publishing 2010, pp. 1–32.
[23] P.K. Mallick, 5 - Thermoplastics and thermoplastic–matrix composites for lightweight automotive structures, in: P.K. Mallick (Ed.), Woodhead Publishing Series in Composites Science and Engineering, Materials, Design and Manufacturing for Lightweight Vehicles, Woodhead Publishing 2010, pp. 174–207.
[24] L.W. McKeen, 1 - Introduction to use of plastics in food packaging, in: Sina Ebnesajjad (Ed.), Plastics Design Library, Plastic Films in Food Packaging, William Andrew Publishing 2013, pp. 1–15.
[25] E. Alfredo Campo, 1 - Polymeric materials and properties, in: E. Alfredo Campo (Ed.), Plastics Design Library, Selection of Polymeric Materials, William Andrew Publishing 2008, pp. 1–39.
[26] J.-H. Lin, et al., Preparation and compatibility evaluation of polypropylene/high density polyethylene polyblends, Materials (Basel, Switzerland) 8 (12) (2015) 8850–8859.
[27] G.X. Wei, et al., Toughening and strengthening of polypropylene using the rigid–rigid polymer toughening concept part I. morphology and mechanical property investigations, Polymer 41 (8) (2000) 2947–2960.
[28] J.J. Andrew, et al., Parameters influencing the impact response of fiber-reinforced polymer matrix composite materials: a critical review, Compos. Struct. 224 (2019) 111007.
[29] M. Valera-Zaragoza, et al., Influence of morphology on the dynamic mechanical characteristics of PP-EP/EVA/organoclay nanocomposites, Compos. Part B 55 (2013) 506–512.
[30] C.G. Martins, et al., Nanocomposites formed from polypropylene/EVA blends, Polymer 50 (7) (2009) 1743–1754.
[31] Zhong-Zhen Yu, et al., Influence of interfacial adhesion on toughening of polyethylene–octene elastomer/nylon 6 blends, J. Appl. Polym. Sci. 69 (9) (1998) 1711–1718.
[32] Jin-Chein Lin, et al., Mechanical behavior of various nanoparticle filled composites at low-velocity impact, Compos. Struct. 74 (1) (2006) 30–36.
[33] T.K. Gupta, et al., Self-sensing and mechanical performance of CNT/GNP/UHMWPE biocompatible nanocomposites, J. Mater. Sci. 53 (11) (2018) 7939–7952.

[34] M.F. Arif, et al., Multifunctional performance of carbon nanotubes and graphene nanoplatelets reinforced PEEK composites enabled via FFF additive manufacturing, Compos. Part B 184 (2020) 107625.
[35] F. Alam, et al., Electrical, mechanical and thermal properties of graphene nanoplatelets reinforced UHMWPE nanocomposites, Mater. Sci. Eng. B 241 (2019) 82–91.
[36] D.K. Rathore, et al., Mechanical performance of CNT-filled glass fiber/epoxy composite in in-situ elevated temperature environments emphasizing the role of CNT content, Compos. A: Appl. Sci. Manuf. 84 (2016) 364–376.
[37] A. Mora, P. Verma, S. Kumar, Electrical conductivity of CNT/polymer composites: 3D printing, measurements and modeling, Compos. Part B 183 (2020) 107600.
[38] T. McNally, et al., Polymer-Carbon Nanotube Composites: Preparation, Properties and Applications, Elsevier, 2011 (Ma, P.-C., et al., Behavior of load transfer in functionalized carbon nanotube/epoxy nanocomposites. Polymer, 2012. 53(26): p. 6081–6088).
[39] S.I. Kundalwal, S. Kumar, Multiscale modeling of stress transfer in continuous microscale fiber reinforced composites with nano-engineered interphase, Mech. Mater. 102 (2016) 117–131.
[40] G. Dong, Y. Tang, Y. Zhao, A survey of modeling of lattice structures fabricated by additive manufacturing, J. Mech. Des. 139 (10) (2017).
[41] Y. Zhai, D.A. Lados, J.L. LaGoy, Additive manufacturing: making imagination the major limitation, J. Miner. 66 (5) (2014) 808–816.
[42] P. Köhnen, et al., Mechanical properties and deformation behavior of additively manufactured lattice structures of stainless steel, Mater. Des. 145 (2018) 205–217.
[43] J. Liljenhjerte, P. Upadhyaya, S. Kumar, Hyperelastic strain measurements and constitutive parameters identification of 3D printed soft polymers by image processing, Addit. Manuf. 11 (2016) 40–48.
[44] A.J. Hart, A. Rao, How to print a 3D object all at once, Science 363 (6431) (2019) 1042–1043.
[45] T. Stanković, J. Mueller, K. Shea, The effect of anisotropy on the optimization of additively manufactured lattice structures, Addit. Manuf. 17 (2017) 67–76.
[46] Shah, T.K., et al., *Carbon nanostructures and methods of making the same*. 2014, Google Patents.
[47] E.G. Gordeev, A.S. Galushko, V.P. Ananikov, Improvement of quality of 3D printed objects by elimination of microscopic structural defects in fused deposition modeling, PLoS One 13 (6) (2018), e0198370, .
[48] R. Juntikka, S. Hallström, Weight-balanced drop test method for characterization of dynamic properties of cellular materials, Int. J. Impact Eng. 30 (5) (2004) 541–554.
[49] P. Verma, et al., Industrially viable technique for the preparation of HDPE/fly ash composites at high loading: thermal, mechanical, and rheological interpretations, J. Appl. Polym. Sci. 135 (11) (2018) 459951.
[50] Y. Zhang, et al., Static and dynamic crushing responses of CFRP sandwich panels filled with different reinforced materials, Mater. Des. 117 (2017) 396–408.
[51] X. Dai, et al., Experimental investigation on the response and residual compressive property of honeycomb sandwich structures under single and repeated low velocity impacts, Mater. Today Commun. 25 (2020) 101309.
[52] Kumar P. Dharmasena, et al., Mechanical response of metallic honeycomb sandwich panel structures to high-intensity dynamic loading, Int. J. Impact Eng. 35 (9) (2008) 1063–1074.
[53] Nan Jin, Fuchi Wang, Yangwei Wang, Bowen Zhang, Huanwu Cheng, Hongmei Zhang, Failure and energy absorption characteristics of four lattice structures under dynamic loading, Mater. Des. 169 (2019) 107655.
[54] G. Choudalakis, A.D. Gotsis, Free volume and mass transport in polymer nanocomposites, Curr. Opin. Colloid Interface Sci. 17 (3) (2012) 132–140.
[55] R.P. White, J.E.G. Lipson, Polymer free volume and its connection to the glass transition, Macromolecules 49 (11) (2016) (p. 39[5187–4007[).
[56] K. Gnanasekaran, et al., 3D printing of CNT- and graphene-based conductive polymer nanocomposites by fused deposition modeling, Appl. Mater. Today 9 (2017) 21–28.
[57] F.N. Habib, et al., Fabrication of polymeric lattice structures for optimum energy absorption using multi jet fusion technology, Mater. Des. 155 (2018) 86–98.
[58] M.J. Al Rifaie, Resilience and Toughness Behavior of 3D-Printed Polymer Lattice Structures: Testing and Modeling, Wright State University, 2017.
[59] X. Cao, et al., Dynamic compressive behavior of a modified additively manufactured rhombic dodecahedron 316L stainless steel lattice structure, Thin-Walled Struct. 148 (2020) 106586.
[60] T. Tancogne-Dejean, et al., High strain rate response of additively-manufactured plate-lattices: experiments and modeling, J. Dyn. Behav. Mater. 5 (3) (2019) 361–375.